

pubs.acs.org/NanoLett Letter

1 Vibrational Coupling Infrared Nanocrystallography

² Richard L. Puro, Thomas P. Gray, Tsitsi A. Kapfunde, George B. Richter-Addo, and Markus B. Raschke*



Cite This: https://doi.org/10.1021/acs.nanolett.3c03958



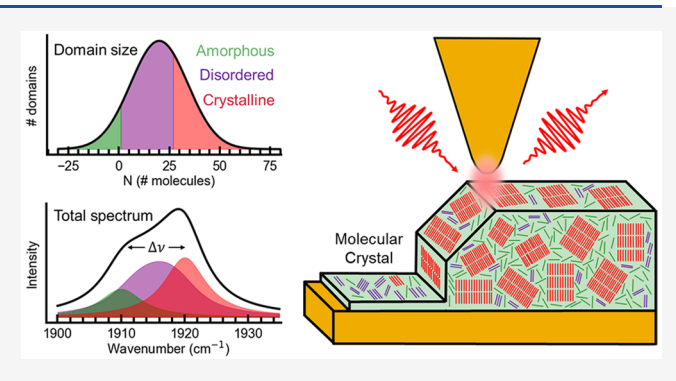
ACCESS I

III Metrics & More

Article Recommendations

s Supporting Information

3 ABSTRACT: Coupling between molecular vibrations leads to 4 collective vibrational states with spectral features sensitive to local 5 molecular order. This provides spectroscopic access to the low-6 frequency intermolecular energy landscape. In its nanospectro-7 scopic implementation, this technique of vibrational coupling 8 nanocrystallography (VCNC) offers information on molecular 9 disorder and domain formation with nanometer spatial resolution. 10 However, deriving local molecular order relies on prior knowledge 11 of the transition dipole magnitude and crystal structure of the 12 underlying ordered phase. Here we develop a quantitative model 13 for VCNC by relating nano-FTIR collective vibrational spectra to 14 the molecular crystal structure from X-ray crystallography. We



15 experimentally validate our approach at the example of a metal organic porphyrin complex with a carbonyl ligand as the probe 16 vibration. This framework establishes VCNC as a powerful tool for measuring low-energy molecular interactions, wave function 17 delocalization, nanoscale disorder, and domain formation in a wide range of molecular systems.

- 18 KEYWORDS: vibrational exciton, transition dipole coupling, infrared spectroscopy,
- 19 scattering scanning near-field optical microscopy (s-SNOM), crystallography

any macroscopic functional properties of molecular **IV** materials are sensitive to the local microscopic environ-22 ment seen by each molecule. Intermolecular coupling of 23 excitons and nanoscale structure influence the photonic and 24 electronic performance of optoelectronic systems, as well as 25 the functionality of proteins and other biological systems. 1-4 26 Similarly, intermolecular coupling of vibrations is important in 27 determining energy and charge transfer on molecular length scales. 5-10 Coupling leads to the emergence of collective 29 vibrations and the delocalization of the vibrational wave 30 function across neighboring molecules, 11,12 with associated 31 changes to vibrational spectra. Eigenmode energies will shift or 32 split depending on the distance, magnitude, and relative 33 orientation of infrared (IR) transition dipoles. 13,14 On one 34 hand, this can lead to seemingly anomalous changes to 35 lineshapes and mode energies in IR vibrational spectrosco-36 py, 15,16 changes to Raman scattering energies or even Raman 37 selection rules, ¹⁷⁻¹⁹ and potential complications in the 38 interpretation of vibrational spectra. ²⁰⁻²² On the other hand, 39 the orientation-dependent spectral features of collective 40 vibrations can be used as a tool to measure local molecular 41 order, disorder, and crystallinity as established only 42 recently. 13,14,23

Due to the interactions between vibrational transition dipoles, accurate interpretation of spectral features in dense molecular systems, such as liquids²¹ or solids, 11,24 relies on modeling. This is commonly performed by calculating the collective eigenmodes that arise from transition dipole

coupling for the vibrations of interest. ^{11,12,24–30} Because of 48 the similarity between the mathematical description of 49 vibrational transition dipole coupling and excitonic dipole 50 coupling, this treatment has conventionally been referred to as 51 the vibrational exciton model (VEM). ¹¹ 52

The VEM has been applied to IR spectroscopy of, e.g., 53 proteins to noninvasively measure their secondary or tertiary 54 structure 26–28,31,32 and molecular aggregates to track crystal- 55 lization and phase changes over time. 24,25,30,33 Raman spectra 56 are also modified by transition dipole coupling, which was 57 demonstrated in surface-enhanced Raman scattering (SERS) of 58 molecular monolayers where collective frequency shifts 59 induced by coupling were related to chemical reaction 60 kinetics. 18 Recently, transition dipole interactions have been 61 probed in small ensembles of molecules by applying the VEM 62 to IR nanoimaging. 13,14,23 This extension of IR vibrational 63 coupling spectroscopy to nanoimaging has established a new 64 technique of all-optical vibrational coupling nanocrystallog- 65 raphy (VCNC), which complements established X-ray and 66 electron based crystallography with its sensitivity to defects and 67 local disorder on the nanoscale.

Received: October 14, 2023 Revised: January 23, 2024 Accepted: January 26, 2024



Nano Letters pubs.acs.org/NanoLett Letter

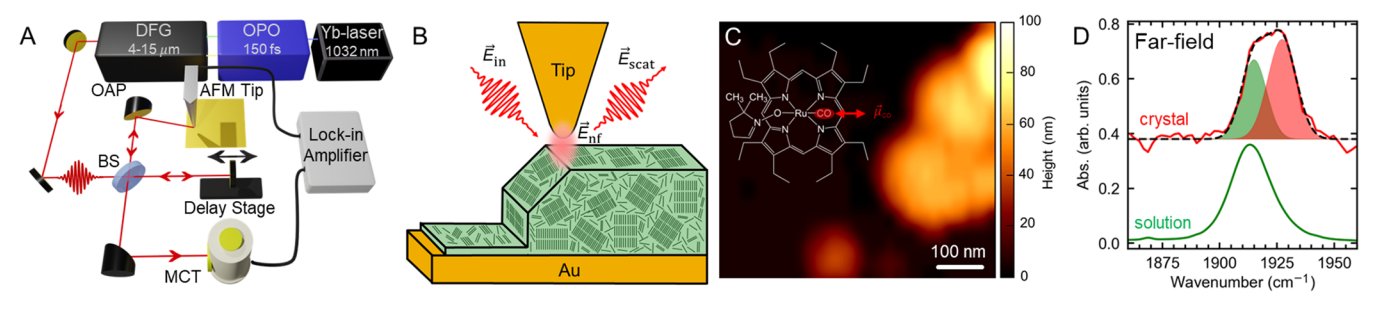


Figure 1. (A) Schematic of nano-FTIR s-SNOM.³⁵ Adapted from ref 13. Copyright 2021 American Chemical Society. (B) Porphyrin (OEP)Ru(CO)(DMPO) nanocrystal with structural defects and thin amorphous film on a gold substrate. (C) Example AFM topography of (OEP)Ru(CO)(DMPO) nanocrystals. Inset: molecular structure of (OEP)Ru(CO) with a carbonyl ligand as the vibrational probe for vibrational coupling nanocrystallography (VCNC). (D) Far-field IR absorption spectra of (OEP)Ru(CO)(DMPO) nanocrystals measured with reflection micro-FTIR (top) and a dilute solution in DCM measured with transmission FTIR (bottom), with Gaussian deconvolution into crystalline and amorphous subpopulations (red and green, respectively).

Previous VCNC studies were based on a qualitative comparison between measured and modeled vibrational lineshapes with modeling based on assumed crystal structures 72 and transition dipole magnitudes used as fit parameters to derive nanoscale disorder. However, without knowing these transition dipole structural parameters, the underlying vibra-75 tional wave function delocalization lengths could not be 76 quantified, leaving an incomplete picture of the accuracy and broader applicability of VCNC. Here we provide a framework 78 for VCNC based on quantitative modeling of collective 79 vibrational spectra using transition dipole structural parameters 80 measured with X-ray diffraction (XRD) and FTIR absorption 81 spectroscopy. The framework is validated at the example of the 82 metal organic porphyrin (OEP)Ru(CO)(DMPO) (OEP = 83 octaethylporphyrinato dianion; DMPO = 5,5-dimethyl-1-84 pyrroline N-oxide) (Figure 1C, inset) as a representative 85 molecular electronic material. We use the carbonyl vibration as 86 a local probe in polycrystalline aggregates of (OEP)Ru(CO)-(DMPO), with the magnitude of the vibrational transition dipole and crystal structure of their highly ordered phase as the only input parameters to quantify the vibrational delocalization 90 lengths. This work thus advances infrared nanocrystallography 91 as a precise molecular ruler, complementing corresponding 92 advances in X-ray and electron microscopies.

93 As established previously, 11,34 the vibrational exciton 94 Hamiltonian for a system of N vibrations is given by

$$\hat{H} = \sum_{i} h v_{i} b_{i}^{\dagger} b_{i} + \sum_{i \neq j} V_{ij} (b_{i}^{\dagger} b_{j} + b_{j}^{\dagger} b_{i})$$

$$= \begin{pmatrix} h v_{1} & V_{12} & \dots & V_{1N} \\ V_{21} & h v_{2} & \dots & V_{2N} \\ \dots & \dots & \dots & \dots \\ V_{N1} & V_{N2} & \dots & h v_{N} \end{pmatrix}$$
(1)

96 where b^{\dagger} and b are the creation and annihilation operators for 97 vibrational excitations, the diagonal term $h\nu_i$ is the vibrational 98 energy of molecule i (treated as degenerate so that $\nu_1 = \nu_2 = ...$ 99 $\equiv \nu$), and the off diagonal terms V_{ij} are the interaction energies 100 between vibrations on different molecules, given by

$$V_{i,j} = \frac{1}{4\pi\varepsilon_0 |\vec{r}_{ij}|^3} \left(\vec{\mu}_i \cdot \vec{\mu}_j - \frac{3(\vec{\mu}_i \cdot \vec{r}_{ij})(\vec{\mu}_j \cdot \vec{r}_{ij})}{|\vec{r}_{ij}|^2} \right)$$
(2)

with $\vec{\mu}_i$ being the transition dipole of vibration i and being the displacement vector between vibrations i and j. We derive the

carbonyl vibrational energy h ν and transition dipole magnitude 104 $|\vec{\mu}_{\rm CO}|$ from IR absorption spectroscopy in dilute solution, and 105 the relative transition dipole positions and orientations \vec{r}_{ij} and 106 $\hat{\mu}_i$ by XRD.

The metalloporphyrin complex (OEP)Ru(II)(CO)- 108 (DMPO) (Figure 1C, inset) was synthesized as described 109 previously. We confirm the structure using a single crystal (~ 110 42 $\times 60 \times 340 \ \mu \text{m}^3$), with XRD performed at 100(2) K (D8 111 Quest κ -geometry diffractometer; Bruker Photon II cmos area 112 detector; Incoatec I μ s microfocus Mo K α source, $\lambda = 0.71073$ 113 Å) (for details, see SI).

IR absorption spectroscopy was performed on solutions of 115 (OEP)Ru(CO)(DMPO) in dichloromethane (DCM), with 116 concentrations ranging from 2.1 to 23 mM, using a commercial 117 FTIR spectrometer (Nicolet iS50 Advanced, Thermo Fisher 118 Scientific) and an IR liquid cell (Pike Technologies) with CaF₂ 119 windows and a 0.1 mm PTFE spacer (Figure 1D, bottom). 120 From the integrated area of the absorption band, expressed as 121 an extinction coefficient $\varepsilon(\nu)$ through Beer's Law, the 122 transition dipole magnitude is calculated as 37,38

$$|\vec{\mu}| = \sqrt{\frac{3\varepsilon_0 h c \ln 10}{2\pi^2 N_A \overline{\nu}}} \int \varepsilon(\nu) d\nu$$
(3) ₁₂₄

with the center frequency of the absorption band $\overline{\nu}=1911$ 125 cm⁻¹ and $N_{\rm A}$ representing Avogadro's number. The transition 126 dipole moment is found to be $|\overline{\mu}_{\rm CO}|=(1.43\pm0.03)~{\rm D}$ (details 127 in SI).

Polycrystalline aggregates of (OEP)Ru(CO)(DMPO) (illus- 129 trated in Figure 1B) with heights ranging from hundreds of 130 nanometers (Figure 1C) to several micrometers (not imaged) 131 were deposited from hexane onto a gold substrate by drop 132 casting. IR s-SNOM (customized nanoIR2-s prototype, Anasys 133 Instruments/Bruker) was performed on these aggregates based 134 on a low-noise tunable femtosecond mid-IR laser source 135 (HarmoniXX difference frequency generation, APE; Levante 136 optical parametric oscillator, APE; Flint Ytterbium pump laser, 137 Light Conversion) with 100 cm⁻¹ fwhm bandwidth and 10 138 mW output power (attenuated to 5 mW) centered at λ = 5.2 139 μ m (1920 cm⁻¹), which was focused onto a metallic AFM tip 140 (Pt/Ir coated, ARROW-NCPt-50, NANO World, tapping at a 141 frequency of 250 kHz).

Ten different nanocrystals (C1–C10) were selected for their 143 well-defined topography and studied in spatio-spectral IR s- 144 SNOM. We apply the VCNC model directly to the imaginary 145 part of the tip-scattered near-field (Re_{NF} + i Im_{NF} = Ae^{$i\phi$}, as 146

Nano Letters pubs.acs.org/NanoLett Letter

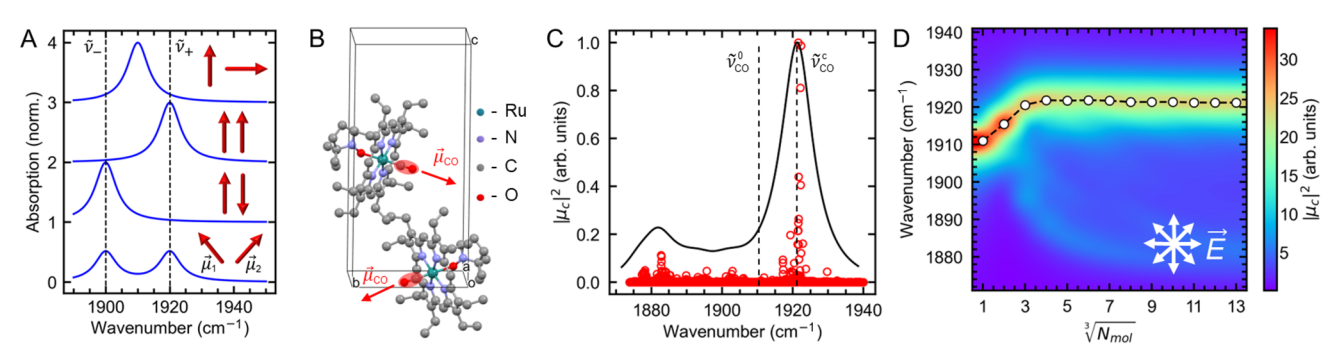


Figure 2. (A) Modeled spectra for dimers with different relative transition dipole orientations. (B) Molecular and crystal structures of DMPO porphyrin with a primitive monoclinic unit cell. The carbonyl ligand is highlighted in red, with arrows denoting the direction of the vibrational transition dipole. (C) Calculated spectrum for a domain with $\sqrt[3]{N} = 13$ molecules. All collective modes (open symbols) result in an emergence of one strongly IR active mode, which is blue-shifted by ~10 cm⁻¹ from the isolated carbonyl vibration (superimposed absorption profile based on Lorentzians with fixed line width of $\Gamma_{\text{FWHM}} = 10 \text{ cm}^{-1}$). (D) Collective frequency shift $\tilde{\nu}_{\text{CO}}^c$ as a function of domain size $(\sqrt[3]{N})$.

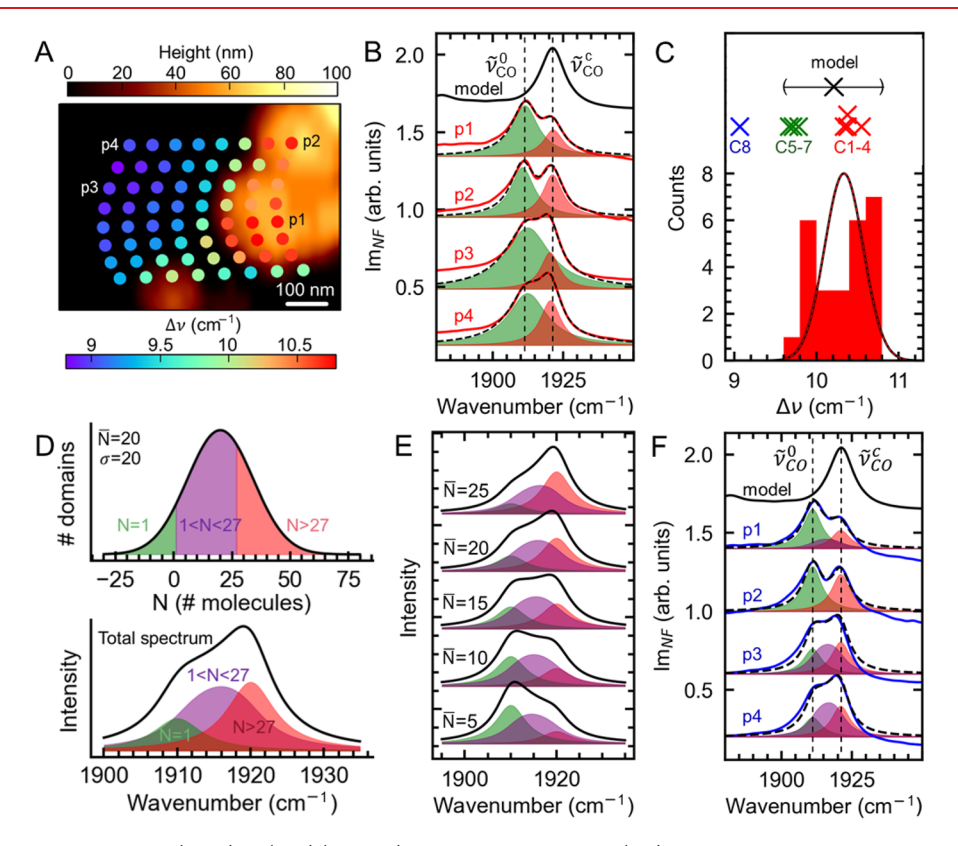


Figure 3. (A) Nano-FTIR imaging of a (OEP)Ru(CO)(DMPO) porphyrin nanocrystal (C1) with spectral shifts of the collective vibrational mode $\Delta\nu$ determined for each point spectrum. (B) Representative point spectra (red) with Lorentzian fits (black, dashed) on more crystalline (p1 and p2) and more amorphous (p3 and p4) regions. (C) Histogram of $\Delta\bar{\nu}$ measured on polycrystalline aggregate C1 with $\Delta\bar{\nu}$ for crystals C1–C8 (denoted by "X") compared to modeling. (D) Gaussian domain size distribution model with mean domain size \bar{N} = 20 and standard deviation σ_N = 20 deconvoluted into domains of single molecules (green), domains with short-range order (purple), and domains with long-range order (red) (top). Corresponding spectrum with respective domain contributions (bottom). (E) Spectral evolution as a function of \bar{N} with σ_N = 20 fixed. (F) Gaussian model fit to spectra from (B) with corresponding spectral deconvolution (for details, see SI).

147 described previously 35,39), valid for small phase responses 148 ($\phi_{\rm max} \lesssim 10^{\circ}$) for which ${\rm Im_{NF}} \ (\tilde{\nu}) \approx \phi(\tilde{\nu}) \approx \kappa$ as is the case 149 here. For larger phase responses, various models to account for 150 the extrinsic tip—sample coupling could be applied. 39,40 151 Figure 1D shows representative micro-FTIR spectra of 152 (OEP)Ru(CO)(DMPO) crystallites in the carbonyl spectral 153 region (top; Nicolet Continuum, Thermo Fisher) in 154 comparison to a solution spectrum (bottom). From a Gaussian 155 deconvolution, it is seen that crystalline (OEP)Ru(CO)-

156 (DMPO) exhibits both a peak at \sim 1911 cm $^{-1}$ and a blue-

shifted peak. We attribute the higher energy peak to the 157 collective carbonyl vibrations from molecules in a crystalline 158 phase and the lower energy peak to uncoupled carbonyl 159 vibrations from molecules in an amorphous phase, correspond- 160 ing to the solution spectrum of isolated molecules.

To predict the collective vibrational spectrum of the $_{162}$ porphyrin crystals as a function of crystaline domain size, we $_{163}$ diagonalize eq 1 numerically to find the eigenenergies and $_{164}$ dipole moments of the collective modes for varying values of $_{165}$ N. The carbonyl atom positions in the two molecules within a $_{166}$

Nano Letters pubs.acs.org/NanoLett Lette

167 unit cell are used to define the positions and relative 168 orientations of the vibrational dipoles. With these coordinates, 169 we construct crystalline domains approximated as equilateral 170 parallelepipeds.

For the polycrystalline aggregates, we expect to measure a polarization-averaged collective spectrum. For a single crystal, only modes with transition dipoles oriented along the tip axis would contribute to the measured spectrum (see SI for the polarization dependence). The calculated polarization-averaged collective energy spectrum for a crystalline ensemble of collective energy spectrum for a crystalline ensemble of molecules of the $N \to \infty$ limit) is shown in Figure 2C, with the uncoupled carbonyl vibration at $\tilde{\nu}^0 = 1911$ cm⁻¹. The spectrum so is dominated by a minority of collective modes, with strong IR activity centered at $\tilde{\nu}^c = 1921$ cm⁻¹. For reasons of symmetry, most collective modes have low or negligible IR activity. Modeled spectra are generated by superimposing Lorentzian Modeled spectra are generated by superimposing Lorentzian absorption profiles for each collective mode with a fixed line width of $\Gamma_{FWHM} = 10$ cm⁻¹ (black solid).

The center frequency of the collective mode is dependent on the number of interacting molecules in each domain N. Figure 2D shows the spectral evolution as a function of $\sqrt[3]{N}$ with $|\vec{\mu}_{CO}|$ is = 1.43 D. It can be seen that the dominant IR-active collective mode at $\tilde{\nu}^c \sim 1921.2$ cm⁻¹ (corresponding to a frequency shift from the uncoupled mode of $\Delta \tilde{\nu}_{mod} = 10.2$ cm⁻¹) rapidly converges already for $\sqrt[3]{N} \geq 3$ with an uncertainty in the large domain limit of $\sigma_N = 0.4$ cm⁻¹. In general, a more continuous shift up to larger values of N is ideal for the VCNC to resolve variations in domain size over a longer range. A nearly constant society domain size. For this model study, however, the negligible dependence of $\tilde{\nu}^c$ on N is desirable for comparison between modeling and experimental results, since the exact domain sizes within the tip near-field are unknown.

The uncertainty σ_N together with the uncertainty in $|\vec{\mu}_{\rm CO}|$ of 203 ± 0.03 D, which translates to an uncertainty in $\Delta \tilde{\nu}_{\rm mod}$ of $\sigma_{\mu} = 204$ 0.4 cm⁻¹ (see SI), leads to a combined uncertainty in $\Delta \tilde{\nu}_{\rm mod}$ of 205 0.6 cm⁻¹, or 6% of the expected energy shift. The expected 206 collective mode shift of $\Delta \tilde{\nu}_{\rm mod} = 10.2 \pm 0.6$ cm⁻¹ can now be 207 compared to measured shifts to determine the deviation 208 between modeling and experiment.

To this end, we perform spatio-spectral IR s-SNOM and 210 extract $\Delta \tilde{\nu}$ for point spectra measured on selected polycrystal-211 line aggregates. Figure 3A shows the locations of the point 212 spectra measured on crystal aggregate C1 and on an adjacent 213 region with flat topography. Spectra are fit using a super-214 position of two Lorentzian absorption profiles, with examples 215 shown in Figure 3B (data red solid, fits dashed black). Symbols 216 in Figure 3A represent the resulting frequency shift, $\Delta \tilde{\nu}$, 217 between the collective and uncoupled mode frequencies. All 218 points on the aggregate exhibit a value of $\Delta \tilde{\nu} \gtrsim 10$ cm⁻¹, with 219 similar results obtained for other aggregates, summarized as a 220 histogram in Figure 3C. The average value of $\Delta \tilde{\nu} = 10.3 \pm 0.3$ 221 cm⁻¹ is in good agreement with the modeled value of $\Delta \tilde{\nu}_{\rm mod} = 222 \ 10.2 \pm 0.6 \ {\rm cm}^{-1}$.

In contrast, nano-FTIR spectra of the flat region adjacent to the aggregate also exhibit a collective vibrational response but with a smaller frequency shift of $\Delta \tilde{\nu} \approx 9~\text{cm}^{-1}$. We interpret this region as a mostly amorphous thin film of (OEP)Ru-227 (CO)(DMPO) deposited along with the apertures during drop casting (illustrated in Figure 1A). Such regions would likely

form small crystalline domains composed of few molecules. In 229 this case, the well-defined crystalline peak may arise from a 230 minority of domains larger than $\sqrt[3]{N} = 3$ (N > 27), while 231 smaller domains would contribute to a broadened background 232 response, distorting the profiles of large domains and domains 233 of isolated molecules.

For these predominantly amorphous regions, we treat the 235 collective vibrational spectra as a superposition of domains 236 assuming a normal distribution of domain sizes with variable 237 average \bar{N} and standard deviation σ_N (Figure 3D, top). Fully 238 disordered domains ($\bar{N} \leq 1$, green) and domains with long- 239 range order ($\bar{N} \geq 27$, red) are represented by Lorentzian 240 profiles with center frequencies 1911 and 1921.2 cm⁻¹, 241 respectively. The intermediate domain responses ($1 < \bar{N} < 242$ 27, purple) are approximated with $\bar{\nu}$ shifting linearly between 243 these two frequencies. The resulting spectrum (Figure 2D, 244 bottom) is then the superposition of these three regions of 245 domain sizes. Resulting model spectra and their domain 246 decompositions are shown in Figure 3E for fixed $\sigma_N = 20$ and 247 varying \bar{N} . We observe a transition from an amorphous to 248 crystalline dominated spectral response with increasing \bar{N} .

We apply this model to points p1-p4 to separate the 250 contributions of fully disordered, partially crystalline, and bulk 251 crystalline domains from the measured spectra (Figure 3F). 252 Spectra are fit by varying only \bar{N} and σ_N . For points p1 and p2, 253 the intermediate domains do not contribute notably to the 254 response, in contrast to points p3 and p4 with corresponding 255 fit parameters $\bar{N}=16$ and 18 and $\sigma_N=23$ and 20, respectively. 256 These results suggest that spectra from regions composed of 257 mostly intermediate domains materialize in a similar way to 258 domains composed of two distinct Lorentzian responses but 259 with narrowed peak splitting.

Additional nano-FTIR spectra of other polycrystalline 261 aggregates (C2-C8) exhibit a similar blue-shifted collective 262 peak spectrally resolved from the uncoupled molecular 263 response. Only two aggregates (C9 and C10) exhibit a purely 264 uncoupled carbonyl response (see Figure S3). Collective mode 265 frequency shifts are consistently below 10.6 cm⁻¹ (Figure 3C, 266 top), in agreement with modeling. The seven aggregates C1- 267 C7 exhibit values of $\Delta \tilde{\nu}$ within the model uncertainty (within 268 6% of $\Delta \tilde{\nu}_{\rm mod}$ = 10.2 cm⁻¹). Crystal C8 exhibits a much lower ²⁶⁹ value of $\Delta \tilde{\nu} \approx 9 \text{ cm}^{-1}$ like the amorphous film region adjacent 270 to aggregate C1. Fits of the Gaussian domain size distribution 271 model to crystal spectra of C5-C8 are shown in the SI and 272 suggest that contributions from intermediate domains are the 273 reason for the narrowed splitting compared to crystals C1-C4. 274 Overall, we find good agreement between VCNC modeling 275 with minimal free parameters and nano-FTIR spectra 276 measured on the range of amorphous and crystalline 277 aggregates.

The porphyrin molecules studied in this work were selected 279 because they crystallize in a lattice that leads to a rapid 280 asymptote of the collective frequency shift. Broader applica- 281 tions of VCNC as a molecular ruler to study order and 282 disorder require a gradual collective mode frequency shift over 283 a larger range of N values, since changes in domain size are not 284 resolvable after the collective shift reaches its asymptote. This 285 raises the question of what lattice structural and vibrational 286 dipole parameters define the dynamic range of VCNC. The 287 spectral mode pattern, degree of collective frequency shift, and 288 its length scale cannot be determined intuitively because of the 289 complex superposition of lattice and orientational effects, 290 which require solving the coupling Hamiltonian numerically 291

Nano Letters pubs.acs.org/NanoLett Lette

292 for a given crystal structure. However, as an example to derive 293 some general trends, we model a simple cubic lattice with 294 transition dipole orientations shown in Figure 4A. We also 295 model a corresponding 2D lattice.

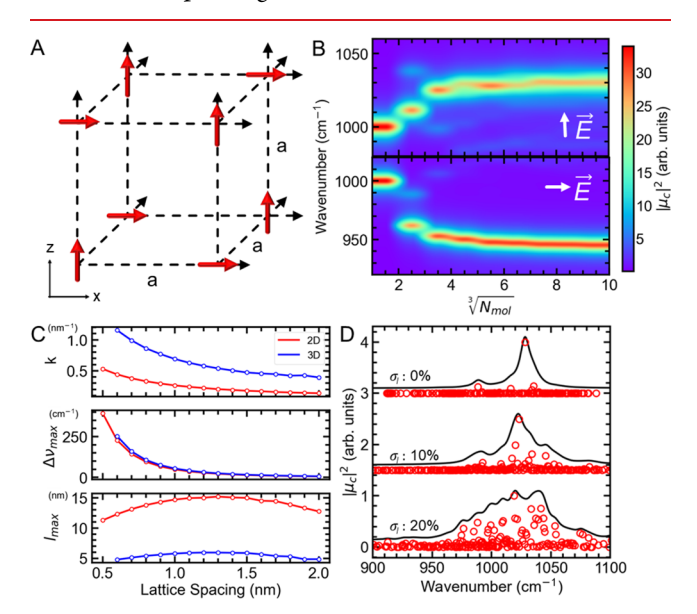


Figure 4. (A) Model structure of transition dipoles arranged in a simple cubic lattice with orientations alternating between the *x*- and *z*-axes. (B) Collective vibrational spectra as a function of domain size when probed parallel to the *z*-axis (top) or *x*-axis (bottom) for a=1 nm and $|\vec{\mu}|=2$ D. (C) Rate k, maximum frequency shift $\Delta\nu_{\max}$ and maximum resolvable domain size l_{\max} as functions of lattice spacing a. (D) Calculated IR spectra (black) and corresponding IR activities of each mode (red) for various degrees of disorder.

Both 3D and 2D lattices exhibit a mode splitting (Figure 297 4B) and a gradual frequency shift with increasing *N*. The two 298 modes are orthogonal to one another, with no modes oriented 299 along the *y*-axis. This is similar to the case of our porphyrin 300 crystal structure, where the blue-shifted collective mode 301 dominates when probing along the crystallographic *b*-axis, 302 whereas a smaller red-shifted mode appears when probing 303 along the *c*-axis (see SI). Therefore, in addition to determining 304 disorder and domain size, in polarization studies of single 305 crystals VCNC also allows for determination of crystal 306 orientation.

To determine the effect of lattice spacing and transition 308 dipole magnitude on the dynamic range of VCNC for this model structure, we vary the lattice spacing from 0.6 to 2 nm 310 and the transition dipole magnitude from 0.5 to 2.0 D (typical values for a range of molecules). The dynamic range is 312 quantified by exponential fits to frequency shifts like what is 313 shown in Figure 4B by the decay constant $k \text{ (nm}^{-1})$ and the 314 maximum frequency shift $\Delta
u_{
m max}$. The maximum resolvable 315 domain size l_{max} is defined as the domain size at which the 316 frequency shift is within 1 cm⁻¹ of $\Delta \nu_{\text{max}}$. From the summary 317 of these values for varying 2D and 3D lattice spacing (Figure 318 4C), we observe a decrease in both k and $\Delta \nu_{\rm max}$ for increasing 319 lattice spacing. These effects compete in their influence on $l_{\rm max}$ 320 to give a peak in the dynamic range for lattice spacings of 1.0 321 to 1.5 nm. The dynamic range $l_{\rm max}$ = 10–15 nm for the 2D 322 system is much higher than l_{max} = 5-6 nm for the 3D system, 323 facilitating domain size measurements up to 20 molecules. 324 The corresponding effect of varying transition dipole moment is shown in the SI, where no variation is observed in k but 325 $\Delta \nu_{\rm max}$ increases with increasing $|\vec{\mu}|$, leading to a monotonic 326 increase in $l_{\rm max}$ with increasing $|\vec{\mu}|$.

Several effects may cause deviations between the measured 328 vibrational response and the response predicted by dipole- 329 dipole interactions modeled here. We approximate the small 330 carbonyl ligand of the otherwise large porphyrin molecule as a 331 simple point dipole and model only the interactions between 332 these dipoles. This simplification neglects the influence of 333 other mobile or polarizable charges, ^{4Y} couplings with other ³³⁴ vibrational modes, ²¹ and higher order multipole interactions. ⁴² ³³⁵ The presence of free carriers may screen the vibrational dipole 336 field, effectively reducing the transition dipole moment 337 compared to isolated molecules when measured in a weakly 338 polarizable dielectric solvent. This effect may be significant in 339 conjugated π -electron systems, but despite the size and 340 complexity of the porphyrin rings studied here, screening 341 from free electrons appeared to only have a negligible effect, as 342 transition dipole interactions account for most of the collective 343 frequency shift. Higher multipole couplings may become 344 relevant for small molecules or otherwise closely spaced 345 vibrational modes when on the order of the dipole length, i.e., 346 few angstroms. However, these higher order interactions would 347 fall off with separation faster than dipole interactions, meaning 348 that, even in systems of very small molecules, higher multipole 349 couplings would likely only be relevant for nearest-neighbor 350 interactions and would cause only an overall shift for larger 351 domains. We expect other solvatochromic effects like a 352 vibrational Stark shift to be negligible in our porphyrin system 353 due to the low polarity and only moderate polarizability of the 354 molecular core, as well as the large separation between polar 355 carbonyl ligands. For highly polar systems, the Stark shift can 356 be included in the vibrational coupling modeling based on, e.g., 357 the Onsager model of solvation. 43 However, the expected net 358 overall spectral shift would only minimally depend on 359 molecular disorder as long as the average intermolecular 360 distance is not affected.⁴³

Deviations in the exact transition dipole structural 362 parameters within the crystalline domains can also change 363 the induced frequency shift. We model this effect at the 364 example of the 3D model structure in Figure 4A by adding 365 random static disorder to each structural parameter. As an 366 example, calculated spectra for varying degrees of disorder in 367 transition dipole position are shown in Figure 4D, with σ_l 368 being the standard deviation of the random disorder 369 (expressed as a percentage of the ideal lattice spacing of 1 370 nm). Disorder breaks the symmetry of the lattice, which results 371 in many additional modes gaining IR activity (with similar 372 effects for disorder in transition dipole magnitude and 373 orientation; see SI). This disorder-induced change of the 374 collective vibrational spectra provides yet another degree of 375 freedom for probing order, disorder, and crystallinity in 376 molecular solids.

In perspective, vibrational coupling nanospectroscopy and 378 nanoimaging provide access to low-frequency energy exchange 379 and vibrational delocalization length, nanoscopic properties 380 that control a wide range of macroscopic material properties. 381 Specifically, vibrational and vibronic coupling influence 382 photosynthetic energy transfer, 44-46 which is limited by 383 recombination at domain boundaries or defects. VCNC of 384 photosynthetic systems could image changes in coupling in the 385 vicinity of these recombination sites, thereby informing 386 material synthesis on a more fundamental level than measure-

Nano Letters pubs.acs.org/NanoLett Letter

388 ments of bulk material properties. Vibrational coupling can 389 also lead to self-trapping of vibrational states, which has been 390 proposed as the energy transport mechanism in proteins and 391 enzymes. 5,47,48 The ability to model and measure vibrational 392 coupling from small molecular ensembles to within single 393 proteins can help to determine energy transfer in biological 394 processes. VCNC and associated vibrational coupling spec-395 troscopy can then be used to measure and imagemolecular 396 disorder and vibrational delocalization, providing insights into 397 charge and energy transfer on the fundamental length and 398 energy scales from which these properties derive. In addition, 399 as a collective excitation with oscillator strength borrowed 400 from all vibrational modes of which it is composed, 49 401 vibrational excitons could hypothetically also serve as a carrier 402 for quantum information. 50 Highly crystalline ensembles of 403 small numbers of molecules could be synthesized, facilitating 404 the preparation of single quanta of vibrations with a large 405 amplitude. Further advancement of VCNC into nonlinear 406 regimes or its application in multimodal approaches may lead 407 to a new understanding of the role vibrations play in a wide 408 range of molecular systems.

9 ASSOCIATED CONTENT

410 Supporting Information

411 The Supporting Information is available free of charge at 412 https://pubs.acs.org/doi/10.1021/acs.nanolett.3c03958.

Additional details on sample preparation and characterization, nano-FTIR measurements, measurements of $|\vec{\mu}|$, spectral fitting with Gaussian domain size distribution model, polarization dependence of collective vibrational spectra, and simulated results for model cubic lattice (PDF)

Data from X-ray diffraction measurements (PDF)

420 AUTHOR INFORMATION

421 Corresponding Author

Markus B. Raschke – Department of Physics and JILA,
University of Colorado, Boulder, Colorado 80309, United
States; Orcid.org/0000-0003-2822-851X;
Email: markus.raschke@colorado.edu

426 Authors

427 Richard L. Puro – Department of Physics and JILA,
 428 University of Colorado, Boulder, Colorado 80309, United
 429 States

Thomas P. Gray – Department of Physics and JILA,
 University of Colorado, Boulder, Colorado 80309, United
 States

Tsitsi A. Kapfunde – Department of Chemistry and
 Biochemistry, University of Oklahoma, Norman, Oklahoma
 73019, United States

George B. Richter-Addo – Department of Chemistry and
Biochemistry, University of Oklahoma, Norman, Oklahoma
73019, United States; orcid.org/0000-0001-9400-0113

439 Complete contact information is available at: 440 https://pubs.acs.org/10.1021/acs.nanolett.3c03958

441 Author Contributions

442 R.L.P., T.P.G., and M.B.R. designed the research; T.A.K. and 443 G.B.R. synthesized samples; T.P.G. contributed modeling 444 tools; R.L.P. performed optical measurements, data analysis, 445 and modeling; and R.L.P. and M.B.R. wrote the manuscript.

Notes

446

447

448

458

The authors declare no competing financial interest.

ACKNOWLEDGMENTS

R.L.P., T.P.G., and M.B.R. acknowledge support by the 449 National Science Foundation (NSF) Science and Technology 450 Center on Real-Time Functional Imaging (STROBE) under 451 Grant DMR 1548924. T.A.K. and G.B.R. acknowledge support 452 from the NSF under Grants CHE-1726630 and CHE- 453 2154603, as well as the University of Oklahoma for funds to 454 purchase the X-ray instrument and computers. The crystal 455 structure was determined by Douglas R. Powell. We thank 456 Roland Wilcken and Eric Muller for helpful discussions.

REFERENCES

- (1) Ross, M. B.; Ku, J. C.; Vaccarezza, V. M.; Schatz, G. C.; Mirkin, 459 C. A. Nanoscale form dictates mesoscale function in plasmonic dna— 460 nanoparticle superlattices. *Nat. Nano.* **2015**, *10*, 453—458.
- (2) Gumyusenge, A.; et al. Semiconducting polymer blends that 462 exhibit stable charge transport at high temperatures. *Science* **2018**, 463 362, 1131–1134.
- (3) Wang, Z.; et al. Disorder induced power-law gaps in an 465 insulator—metal mott transition. *Proc. Natl. Acad. Sci. U. S. A.* **2018**, 466 115, 11198—11202.
- (4) Mao, X.; et al. Self-assembled nanostructures in ionic liquids 468 facilitate charge storage at electrified interfaces. *Nat. Mater.* **2019**, *18*, 469 1350–1357.
- (5) Edler, J.; Pfister, R.; Pouthier, V.; Falvo, C.; Hamm, P. Direct 471 observation of self-trapped vibrational states in α -helices. *Phys. Rev.* 472 *Lett.* **2004**, 93, 106405.
- (6) Tiwari, V.; Peters, W. K.; Jonas, D. M. Electronic resonance with 474 anticorrelated pigment vibrations drives photosynthetic energy 475 transfer outside the adiabatic framework. *Proc. Natl. Acad. Sci. U. S.* 476 *A.* 2013, 110, 1203–1208.
- (7) Nelson, T. R.; et al. Coherent exciton-vibrational dynamics and 478 energy transfer in conjugated organics. *Nat. Commun.* **2018**, *9*, 2316. 479
- (8) Chin, A. W.; et al. The role of non-equilibrium vibrational 480 structures in electronic coherence and recoherence in pigment— 481 protein complexes. *Nat. Phys.* **2013**, *9*, 113–118.
- (9) Hestand, N. J.; Spano, F. C. Expanded theory of h-and j- 483 molecular aggregates: the effects of vibronic coupling and 484 intermolecular charge transfer. *Chem. Rev.* **2018**, *118*, 7069–7163. 485
- (10) Sneyd, A. J.; et al. Efficient energy transport in an organic 486 semiconductor mediated by transient exciton delocalization. *Sci. Adv.* 487 **2021**, *7*, No. eabh4232.
- (11) Dows, D. A. Intermolecular coupling of vibrations in molecular 489 crystals. *J. Chem. Phys.* **1960**, 32, 1342–1347.
- (12) Kasha, M. Energy Transfer Mechanisms and the Molecular 491 Exciton Model for Molecular Aggregates. *Radiat. Res.* **1963**, 20, 55–492 70.
- (13) Gray, T. P.; Nishida, J.; Johnson, S. C.; Raschke, M. B. 2D 494 Vibrational Exciton Nanoimaging of Domain Formation in Self-495 Assembled Monolayers. *Nano Lett.* **2021**, *21*, 5754–5759.
- (14) Muller, E. A.; et al. Vibrational exciton nanoimaging of phases 497 and domains in porphyrin nanocrystals. *Proc. Natl. Acad. Sci. U. S. A.* 498 **2020**, *117*, 7030–7037.
- (15) Trzebiatowska-Gusowska, M.; Piela, K.; Misiaszek, T.; Szostak, 500 M. M.; Baran, J. The revision of intermolecular interactions in 1,3- 501 dinitrobenzene crystal The role of nitro groups in optical 502 nonlinearity. *J. Raman Spectrosc.* **2010**, *41*, 1338–1347.
- (16) Levinson, N. M.; Fried, S. D.; Boxer, S. G. Solvent-induced 504 infrared frequency shifts in aromatic nitriles are quantitatively 505 described by the vibrational stark effect. *J. Phys. Chem. B* **2012**, *116*, 506 10470–10476.
- (17) Cançado, L. G.; Beams, R.; Jorio, A.; Novotny, L. Theory of 508 spatial coherence in near-field raman scattering. *Phys. Rev. X* **2014**, *4*, 509 031054.

Nano Letters pubs.acs.org/NanoLett Lette

- 511 (18) Mueller, N. S.; et al. Collective Mid-Infrared Vibrations in 512 Surface-Enhanced Raman Scattering. *Nano Lett.* **2022**, 22, 7254–513 7260.
- 514 (19) Beams, R.; Cançado, L. G.; Oh, S.-H.; Jorio, A.; Novotny, L. 515 Spatial coherence in near-field raman scattering. *Phys. Rev. Lett.* **2014**, 516 *113*, 186101.
- 517 (20) Fried, S. D.; Boxer, S. G. Measuring electric fields and 518 noncovalent interactions using the vibrational stark effect. *Acc. Chem.* 519 *Res.* **2015**, *48*, 998–1006.
- 520 (21) Fica-Contreras, S. M.; Charnay, A. P.; Pan, J.; Fayer, M. D. 521 Rethinking vibrational stark spectroscopy: Peak shifts, line widths, and 522 the role of non-stark solvent coupling. *J. Phys. Chem. B* **2023**, *127*, 523 717–731.
- 524 (22) Chen, Z.; et al. Tracing the crystallization process of 525 polyoxymethylene/poly(ethylene oxide) crystalline/crystalline blends 526 by two-dimensional infrared correlation spectroscopy. *Vib. Spectrosc.* 527 **2012**, 62, 299–309.
- 528 (23) Donges, S. A.; et al. Multidimensional nano-imaging of 529 structure, coupling, and disorder in molecular materials. *Nano Lett.* 530 **2021**, *21*, 6463–6470.
- 531 (24) Signorell, R. Verification of the vibrational exciton approach for 532 CO2 and N2O nanoparticles. *J. Chem. Phys.* **2003**, *118*, 2707–2715.
- 533 (25) Sigurbjörnsson, Ó. F.; Firanescu, G.; Signorell, R. Vibrational 534 exciton coupling as a probe for phase transitions and shape changes of
- 535 fluoroform aerosol particles. Phys. Chem. Chem. Phys. 2009, 11, 187-536 194.
- 537 (26) Abramavicius, D.; Zhuang, W.; Mukamel, S. Peptide secondary 538 structure determination by three- pulse coherent vibrational spectros-
- 539 copies: A simulation study. *J. Phys. Chem. B* **2004**, *108*, 18034–18045. 540 (27) Gorbunov, R. D.; Kosov, D. S.; Stock, G. Ab initio-based
- s41 exciton model of amide I vibrations in peptides: Definition, s42 conformational dependence, and transferability. *J. Chem. Phys.* **2005**, s43 122, 224904.
- 544 (28) Małolepsza, E.; Straub, J. E. Empirical maps for the calculation 545 of amide I vibrational spectra of proteins from classical molecular 546 dynamics simulations. *J. Phys. Chem. B* **2014**, *118*, 7848–7855.
- 547 (29) Reppert, M.; Tokmakoff, A. Electrostatic frequency shifts in 548 amide i vibrational spectra: Direct parameterization against experisely ment. *J. Chem. Phys.* **2013**, *138*, 134116.
- 550 (30) Kobayashi, M.; Sakashita, M. Morphology dependent 551 anomalous frequency shifts of infrared absorption bands of polymer 552 crystals: Interpretation in terms of transition dipole-dipole coupling 553 theory. *J. Chem. Phys.* **1992**, *96*, 748–760.
- 554 (31) Moran, A.; Mukamel, S. The origin of vibrational mode 555 couplings in various secondary structural motifs of polypeptides. *Proc.* 556 *Natl. Acad. Sci. U. S. A.* **2004**, *101*, 506–510.
- 557 (32) La Cour Jansen, T.; Dijkstra, A. G.; Watson, T. M.; Hirst, J. D.; 558 Knoester, J. Modeling the amide I bands of small peptides. *J. Chem.* 559 *Phys.* **2006**, *125*, 044312.
- 560 (33) Tanabe, Y.; Shimomura, M. A2Mode Vibration in Infrared 561 Absorption Spectrum of Trigonal Poly(oxymethylene). *Macro-s62 molecules* **1990**, 23, 5031–5034.
- 563 (34) Hamm, P.; Zanni, M. Concepts and methods of 2D infrared 564 spectroscopy; Cambridge University Press: Cambridge, UK, 2012.
- 565 (35) Muller, E. A.; Pollard, B.; Raschke, M. B. Infrared chemical 566 nano-imaging: Accessing structure, coupling, and dynamics on
- 567 molecular length scales. *J. Phys. Chem. Lett.* **2015**, *6*, 1275–1284. 568 (36) Lee, J.; Twamley, B.; Richter-Addo, G. B. Nitrones are suitable
- 569 ligands for heme models: X-ray crystal structure of the first 570 metalloporphyrin nitrone complex. *Chem. Commun.* **2002**, 380–381.
- 571 (37) Andrews, S. S.; Boxer, S. G. Vibrational stark effects of nitriles i.
- 572 methods and experimental results. *J. Phys. Chem. A* **2000**, *104*, 573 11853–11863.
- 574 (38) Atkins, P. Physical Chemistry, 5th ed.; W. H. Freeman and 575 Company: New York, NY, 1994).
- 576 (39) Muller, E. A.; Pollard, B.; Bechtel, H. A.; van Blerkom, P.; 577 Raschke, M. B. Infrared vibrational nanocrystallography and nano-
- 578 imaging. Sci. Adv. 2016, 2, No. e1601006.

- (40) Govyadinov, A. A.; Amenabar, I.; Huth, F.; Carney, P. S.; 579 Hillenbrand, R. Quantitative measurement of local infrared absorption 580 and dielectric function with tip-enhanced near-field microscopy. 581 journal of physical chemistry letters 2013, 4, 1526–1531.
- (41) Ohta, T.; et al. Interlayer interaction and electronic screening in 583 multilayer graphene investigated with angle-resolved photoemission 584 spectroscopy. *Phys. Rev. Lett.* **2007**, *98*, 206802. 585
- (42) Wang, L.; et al. Quadrupole contribution of c o vibrational 586 band in sum frequency generation spectra of organic carbonates. J. 587 Phys. Chem. Lett. 2020, 11, 8527–8531.
- (43) Pollard, B.; Muller, E. A.; Hinrichs, K.; Raschke, M. B. 589 Vibrational nano-spectroscopic imaging correlating structure with 590 intermolecular coupling and dynamics. *Nat. Commun.* **2014**, *5*, 1–7. 591
- (44) Tiwari, V.; Peters, W. K.; Jonas, D. M. Electronic resonance 592 with anticorrelated pigment vibrations drives photosynthetic energy 593 transfer outside the adiabatic framework. *Proc. Natl. Acad. Sci. U. S. A.* 594 **2013**, *110*, 1203–1208.
- (45) Yeh, S.-H.; Hoehn, R. D.; Allodi, M. A.; Engel, G. S.; Kais, S. 596 Elucidation of near-resonance vibronic coherence lifetimes by 597 nonadiabatic electronic-vibrational state character mixing. *Proc. Natl.* 598 *Acad. Sci. U. S. A.* **2019**, *116*, 18263–18268.
- (46) Higgins, J. S.; et al. Photosynthesis tunes quantum-mechanical 600 mixing of electronic and vibrational states to steer exciton energy 601 transfer. *Proc. Natl. Acad. Sci. U. S. A.* **2021**, *118*, No. e2018240118. 602
- (47) Davydov, A. S. The theory of contraction of proteins under 603 their excitation. *J. Theor. Biol.* **1973**, 38, 559–569.
- (48) Schwartz, E.; et al. Self-trapped vibrational states in synthetic β 605 sheet helices. *Chem. Commun.* **2009**, 4675–4677.
- (49) Pouthier, V. Vibrational exciton mediated quantum state 607 transfer: Simple model. *Phys. Rev. B* **2012**, *85*, 214303.
- (50) Tesch, C. M.; de Vivie-Riedle, R. Quantum computation with 609 vibrationally excited molecules. *Physical review letters* **2002**, 89, 610 157901.